IEEE Access
Multidisciplinary : Rapid Review : Open Access Journal

Received 25 March 2026, accepted 2 May 2026, date of publication 5 May 2026, date of current version 8 May 2026.
Digital Object Identifier 10.1109/ACCESS.2026.3690562

RESEARCH ARTICLE

Dual-Polarized Super-Wideband Antenna With Artificial Materials-Enhanced Gain for 5G Millimeter-Wave and Remote Sensing Applications

BASHAR A. F. ESMAIL[1], (Member, IEEE), DUSTIN ISLEIFSON[1], (Senior Member, IEEE), SLAWOMIR KOZIEL[2,3], (Fellow, IEEE), AND ANNA PIETRENKO-DABROWSKA[3], (Senior Member, IEEE)
[1]Department of Electrical and Computer Engineering, University of Manitoba, Winnipeg, MB R3T 5V6, Canada
[2]Department of Engineering, Reykjavík University, 102 Reykjavík, Iceland
[3]Faculty of Electronics, Telecommunications and Informatics, Gdańsk University of Technology, 80-233 Gdańsk, Poland

Corresponding author: Slawomir Koziel (koziel@ru.is)

This work was supported in part by Icelandic Centre for Research under Grant 2410297, and in part by the National Science Centre of Poland under Grant 2022/47/B/ST7/00072.

ABSTRACT This paper presents a high-performance dual-polarized super-wideband (SWB) antenna that employs optimized slots and an Artificial Material (AM) array to achieve remarkable enhancements in both bandwidth and gain. The proposed design features a compact Vivaldi configuration with integrated arrow-shaped slots, enabling SWB operation while maintaining a low-profile size of $0.66 \times 0.49 \times 0.01\ \lambda^3$. A constrained trust-region gradient-based optimization is used to refine the slot geometry and antenna parameters, achieving an operating range from 8.4 to 42.8 GHz with a stable gain of approximately 10 dBi at frequencies above 17 GHz. The incorporation of AMs further enhances the gain and extends the bandwidth. The AM antenna, with dimensions of $0.94 \times 0.49 \times 0.01\ \lambda^3$, achieves peak gains of 13.3 dBi at 24 and 38 GHz and covers a wide operating range of 8.3–45 GHz. Dual polarization is realized by employing two orthogonally oriented Vivaldi elements, resulting in a high polarization isolation exceeding 25 dB across the entire operating bandwidth. The experimental results demonstrate excellent agreement with the simulation-based findings. Featuring SWB performance, high gain, strong polarization isolation, polarization diversity, and a compact low-profile structure, the proposed antenna is well suited for 5G millimeter-wave (MMW) and satellite remote sensing applications.

INDEX TERMS AMs, antenna optimization, dual-polarization antenna, millimeter-wave, remote sensing.

I. INTRODUCTION

The growing demand for multifunctional antennas in compact platforms—such as 5G millimeter-wave (MMW) communication systems, CubeSats, and unmanned aerial vehicles (UAVs)—has driven extensive research in designing antennas that combine wide bandwidth, high gain, and polarization diversity. In particular, applications such as 5G wireless networks and satellite-based remote sensing require antennas capable of providing broad impedance bandwidth, strong directional gain, and dual polarization to ensure reliable signal reception, enhanced data throughput, and adaptability to diverse operational environments. The Vivaldi antenna—first introduced by Gazit [1]—has emerged as a leading solution for compact, high-performance systems, offering efficient end-fire radiation, inherently wide bandwidth, stable patterns, and a low-profile design compatible with high-frequency PCB technologies. These features make

The associate editor coordinating the review of this manuscript and approving it for publication was Ahmed Almradi.

the Vivaldi antenna particularly suitable for modern 5G MMW systems. The 3rd Generation Partnership Project (3GPP) has allocated several MMW frequency bands for 5G, including n257 (26.5–29.5 GHz), n258 (24.25–27.5 GHz), n259 (39.5–43.5 GHz), n260 (37–40 GHz), and n261 (27.5–28.35 GHz) [2]. Furthermore, the Ku and K bands have attracted significant interest in the context of satellite remote sensing applications [3], [4], underscoring the importance of wideband, high-performance antenna solutions such as the Vivaldi.

A variety of techniques have been investigated to enhance the performance of Vivaldi antennas, particularly in terms of bandwidth and gain. Common approaches include incorporating corrugations along the flares, introducing slots within the antenna structure, and utilizing ridged substrate-integrated waveguides. These methods have proven effective in extending the operational bandwidth and enhancing radiation performance while maintaining a compact form factor. The incorporation of corrugated and slotted structures into Vivaldi antenna designs has been shown to effectively enhance bandwidth by facilitating the formation of current loops between adjacent slots. These loops lower the surface impedance, thereby improving impedance matching and broadening the overall bandwidth [5], [6], [7], [8], [9], [10], [11], [12], [13]. Several studies have investigated different corrugation geometries to assess their influence on antenna performance. Among these, rectangular corrugation slots have demonstrated the most significant improvements in bandwidth, while sawtooth and elliptical shapes yielded moderate enhancements [8], [9], [10]. Circular [11] and rectangular [12] slots, when strategically positioned along the radiating edges, have been reported to enhance the bandwidth from 6–12 GHz to –12 GHz and from 7.–18 GHz to –18 GHz, respectively. Similarly, in [13], symmetrically etched elliptical slots along the radiating edges extended the bandwidth from 7.4–18.0 GHz to 5.–18.0 GHz. While notable advancements have been achieved, identifying the optimal slot geometry and placement remains complex due to the lack of an exact analytical model. As a result, the process relies heavily on manual tuning and empirical adjustments, which are time-consuming and inefficient. To address this challenge, this study introduces an optimization-based approach to facilitate slot design, thereby enhancing precision and reducing design effort.

In addition to bandwidth enhancement, improving antenna gain has been a major focus of recent research. Conventional approaches to achieve higher gain typically involve antenna arrays, three-dimensional (3D) or multilayer-stacked configurations, and dielectric lens structures [14], [15], [16], [17]. Although these methods can provide considerable gain improvement, they often increase the overall size, structural complexity, and feed network losses. As an alternative, artificial materials (AMs)—such as metamaterials (MMs) and metasurfaces (MS)—have emerged as an effective and cost-efficient solution that enhances gain performance without significantly enlarging the antenna footprint [18], [19]. Integrating these structures into antenna designs has been shown to significantly enhance gain performance while maintaining a compact form factor [20], [21], [22], [23]. In [20], an antipodal Vivaldi antenna integrated with a square-shaped split-ring resonator (SSRR) demonstrated improved gain across 34–43.8 GHz, achieving a peak gain of 10.4 dBi near 41 GHz. Similarly, an MM-based Vivaldi antenna operating from 1.4 to 2.1 GHz was reported in [21], where strategically placed unit cells along the flare region increased the gain to 10.5 dBi at 2 GHz. In [22], the incorporation of a double E-shaped MM structure within the flare region enhanced the antenna's gain over 13–20 GHz, achieving a maximum of 12.4 dBi at 19.5 GHz. The incorporation of MS unit cells, as reported in [23], enabled a realized gain of 11.8 dBi across a wide operating bandwidth from 3.7 to 25 GHz.

Dual-polarized Vivaldi antenna designs have received comparatively limited attention in the literature [24], [25]. In [24], two orthogonally oriented elements achieved dual polarization with 20 dB isolation over 22.5–45 GHz and a maximum gain of 8.5 dBi. Similarly, in [25], orthogonal elements provided 23 dB isolation across 1.8–6 GHz with a peak gain of 10 dBi. Both designs employed complex feed structures to avoid transmission line intersection, resulting in higher design complexity, relatively narrow bandwidths, and large antenna sizes. Dual-polarized patch and dipole antennas designed for 5G MMW applications [2], [26] exhibit moderate isolation and gain—14 dB/13 dBi [26] and 13 dB/10 dBi [2], respectively. However, these designs rely on multilayer structures, which increase fabrication complexity and overall system cost. In contrast, a dual-polarized horn antenna reported in [27] achieves a gain of 8 dBi along with isolation exceeding 17.5 dB over the 5.08–6.4 GHz frequency range, offering a simpler architecture but at lower gain levels.

This study proposes a dual-polarized Vivaldi antenna integrating strategically designed slots and AM elements to enhance impedance bandwidth and gain performance. The slots effectively broaden the bandwidth without increasing the antenna's physical footprint, while the AMs within the aperture enable efficient beam shaping, improved gain, and compensation for MMW path loss.The antenna also exhibits high polarization isolation, a key requirement for systems employing orthogonal polarizations in communication and sensing applications, enabling simultaneous independent data streams through dual-polarized operation. Simulation results demonstrate a wide impedance bandwidth from 8.3 to 45 GHz, with high gain across both polarization ports. This SWB operation is physically realized by exploiting the non-resonant, progressive radiation mechanism of the tapered slot topology. Broadband stability is achieved through the optimized combination of the feed transition, arrow-shaped slots that enhance impedance matching at lower frequencies, and an AM array that enhances gain and extends the effective operating bandwidth at higher frequencies.

Experimental results confirm that the proposed design maintains robust SWB performance under practical fabrication tolerances. Moreover, the isolation between the two ports exceeds 25 dB throughout the band, ensuring reliable polarization diversity performance. The continuous 8.3–45 GHz bandwidth encompasses all key 5G MMW bands, making the proposed SWB dual-polarized Vivaldi antenna highly suitable for 5G systems. Owing to its low-profile planar structure and compact form factor, the antenna can be readily integrated into phased arrays and small-cell modules while maintaining high gain and strong isolation. With its compact structure, wide bandwidth, high gain, and strong isolation, the proposed design offers a promising solution for dual-function platforms supporting high-resolution remote sensing and high-data-rate 5G communications. The primary contributions of this research are outlined below:

I. Development of a SWB Vivaldi antenna operating across the microwave and MMW bands for emerging 5G and satellite remote sensing applications, achieving an enhanced bandwidth of 8.4–42.8 GHz and ~10 dBi gain through the integration of arrow-shaped slots optimized using the trust-region gradient-based optimization technique.

II. Design of an AMs incorporated into the antenna to further enhance gain and bandwidth performance, achieving 13.4 dBi at 38 GHz within an operating range of 8.3–45 GHz.

III. Realization of a dual-polarized Vivaldi antenna exhibiting nearly identical reflection and radiation characteristics for both polarizations, with polarization isolation exceeding 25 dB.

II. VIVALDI ANTENNA DESIGN

The design process begins with a conventional Vivaldi antenna as the baseline, after which slots are introduced to enhance performance. The proposed antenna configuration is shown in Fig. 1. The exponential taper profile of the aperture, defined by (1), determines the slope of the tapered slot and governs the radiation behavior across the operating frequency range:

$$y(x) = \pm V e^{R \cdot x} \tag{1}$$

where V represents half of the minimum width of the tapered slot (W_m), and R denotes the taper's rate. The variable x corresponds to the position along the tapered slot length (L_{tap}). Both the taper rate R and the taper length L_{tap} play a critical role in determining the antenna's performance. For optimal performance, the taper length L_{tap} should satisfy the condition [28]:

$$L_{\mathrm{tap}} > \lambda_g \tag{2}$$

The guided wavelength λ_g is calculated based on the effective dielectric constant ε_{eff} and the operating frequency using the standard relation $\lambda_g = c/(f \times \sqrt{\varepsilon_{eff}})$. The upper-edge mouth opening between the flares, denoted by W_x, is preferably chosen within the following bounds to maintain desirable electromagnetic performance [29]:

$$W_{x1} < W_x < W_{x2} \tag{3}$$

where

$$W_{x1} \approx \lambda_0 \quad at\ f = 26 \text{ GHz} \tag{4}$$

and

$$W_{x2} \approx \lambda_m/2 \tag{5}$$

where λ_m is calculated at the lower frequency f_L =8.4 GHz. As shown in Fig. 1, W_f denotes the width of the microstrip feed line, with its length corresponding to half of the total antenna width ($W/2$) plus an extended stub section. The parameter C_u represents the remaining unslotted copper length along the x-axis. The antenna is excited through electromagnetic coupling between the microstrip line and the slot line. The microstrip line was placed on the backside of the substrate, and a stub structure characterized by θ and L_s was employed at its termination to achieve sufficient impedance matching. This transition must be carefully engineered to ensure efficient impedance matching between the low-impedance microstrip line and the high-impedance slot line. Proper design of this interface enhances the overall bandwidth performance. The antenna structure was implemented on a Rogers RT5880 substrate, characterized by a dielectric constant ε_r of 2.2. The substrate thickness is 0.38 mm, with a 0.035 mm copper layer used for metallization. With overall dimensions of $0.66 \times 0.49 \times 0.01\ \lambda^3$, the antenna exhibits a compact design well suited for space-limited high-frequency communication and remote sensing systems. The proposed antenna structure was simulated, and the results—obtained after multiple iterations of manual optimization—are shown in Fig. 2. The antenna operates effectively across four distinct frequency bands: 9.3–11.8 GHz, 13.5–15.7 GHz, 16.7–21.6 GHz and 22.1–41.5 GHz. To enhance the overall impedance bandwidth without increasing the physical dimensions, a series of arrow-shaped slots was incorporated into the antenna structure, as illustrated in Fig. 1. The arrow-shaped slot is a composite parametric geometry rather than a single closed-form equation. Its shape is defined by the combination of two geometric primitives. The rectangular tail is specified by lengths L_i for $i = 1, 2, 3, \ldots, 11$ and width W_1. The semi-elliptical head is defined by the standard elliptical equation $x^2/a^2 + y^2/b^2 = 1$, where $a = L_x$ (semi-minor axis) and $b = L_y$ (semi-major axis). The half-ellipse is then merged with the rectangular tail to form the complete arrow shape.

Figure 2 presents the simulated reflection coefficient, S_{11}, of the slotted antenna prior to optimization. The results demonstrate a bandwidth improvement, yielding operating bands of 9.3–10 GHz, 13–14.9 GHz, and 15.5–42.8 GHz, thereby indicating significant potential for further optimization of the operating spectrum. Although the introduction of arrow-shaped slots increases the geometric complexity of the baseline Vivaldi configuration, this modification was essential to achieve enhanced bandwidth performance while preserving the antenna's highly compact physical footprint, which is critical for space-constrained applications. Given the wide operational bandwidth, the manual optimization process was time-consuming and required human intervention after

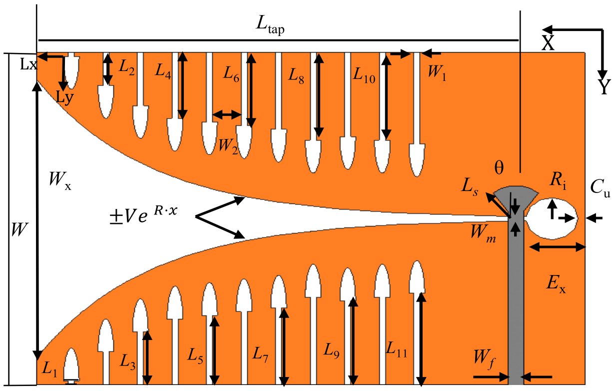

FIGURE 1. Structural layout and key dimensions of the Vivaldi antenna incorporating slots, dimensions: $W = 18$ mm, $W_x = 15.60$ mm, $L_{tap} = 21$ mm, $E_x = 3.000$ mm, $L_x = 0.350$ mm, $L_y = 2.210$ mm, $R = 0.195$ mm, $W_1 = 0.210$mm, $W_2 = 1.250$ mm, $W_m = 0.240$ mm, $L_1 = 0.200$ mm, $L_2 = 1.840$ mm, $L_3 = 2.920$ mm, $L_4 = 3.610$ mm, $L_5 = 3.790$ mm, $L_6 = 4.110$ mm, $L_7 = 4.230$ mm, $L_8 = 4.790$ mm, $L_9 = 4.600$ mm, $L_{10} = 4.810$ mm, $L_{11} = 4.980$ mm, $W_f = 0.910$ mm, $L_s = 1$ mm, $\theta = 90°$, $R_i = 1.15$ mm, $C_u = 0.300$ mm.

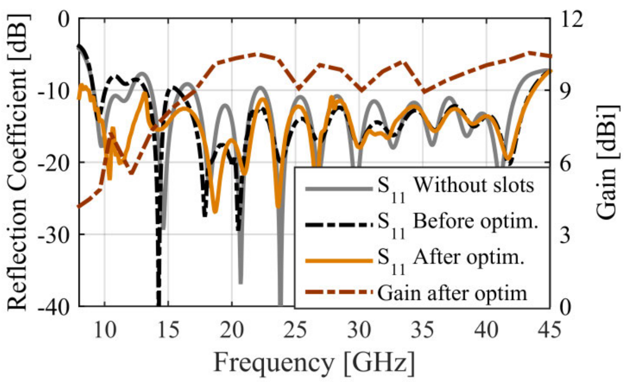

FIGURE 2. Reflection coefficients of the antenna in three cases: without slots, before optimization, and after optimization, along with the corresponding gain after optimization.

each iteration. Moreover, no precise or systematic method exists for determining the slot dimensions and locations. These limitations motivated the adoption of a numerical optimization approach in the subsequent design phase to further enhance performance, particularly after incorporating the slot structures. The details of the numerical optimization process are presented in Section III.

III. VIVALDI ANTENNA OPTIMIZATION

Traditional approaches, such as parameter sweeping or interactive tuning of the antenna geometry, are often insufficient for identifying an optimal configuration due to the complex interactions among design parameters and the wide operational bandwidth. To address these limitations, a trust-region (TR) gradient-based numerical optimization approach—focusing on slot-related parameters known to have a major impact on impedance bandwidth—was implemented, as detailed below. The TR framework was specifically selected for its superior computational efficiency, deterministic convergence, and robustness in solving such highly nonlinear wideband antenna problems. Compared to global heuristics, it significantly reduces the cost of expensive full-wave electromagnetic simulations; compared to standard gradient methods, it offers improved stability through adaptive step-size control. Furthermore, unlike manual parameter sweeping, the TR algorithm efficiently handles high-dimensional and strongly coupled design variables, ensuring an optimal solution that accounts for the intricate electromagnetic interdependencies within the antenna structure. The primary aim of the optimization process was to ensure efficient impedance matching throughout the 8.4–42.8 GHz frequency range, thereby covering a substantial portion of the microwave spectrum and extending into the MMW region. Specifically, the design aimed to satisfy the condition $|S_{11}(\boldsymbol{x}, f)| \leq -10$ for all $f \in F = [8.4\ 42.8]$ GHz, where $\boldsymbol{x}$ is the vector of tunable design variables. The set of designable parameters was grouped into a vector $\boldsymbol{x} = [R, L_x, L_y, L_1, L_2, L_3, L_4, L_5, L_6, L_7, L_8, L_9, L_{10}, L_{11}, W_1, W_f]^T$, as illustrated in Fig. 1. The optimization was carried out over the design space X, defined by the following bounds: $0.18 \leq R \leq 0.21$ mm, $0.2 \leq L_x \leq 0.5$ mm, $0.5 \leq L_y \leq 2.3$ mm, $0.2 \leq L_1 \leq 0.3$, $0.2 \leq L_2 \leq 2$, $0.2 \leq L_3 \leq 3$, $0.2 \leq L_4 \leq 4$, $0.2 \leq L_5 \leq 4.4$, $0.2 \leq L_6 \leq 4.6$, $0.2 \leq L_7 \leq 4.9$, $0.2 \leq L_8 \leq 5$, $0.2 \leq L_9 \leq 5.2$, $0.2 \leq L_{10} \leq 5.4$, $0.2 \leq L_{11} \leq 5.5$, $0.2 \leq W_1 \leq 0.5$ mm, and $0.3 \leq W_f \leq 1$ mm. In addition to these bounds, several geometric constraints were imposed to preserve the physical integrity of the antenna: W_m and L_1 through $L_{11} \geq 0.2$ mm (The minimum value of 0.2 mm is determined by manufacturing requirements). The range of R is determined through a parametric study to ensure that the condition $W_{x1} = \lambda_0 < W_x < W_{x2} = \lambda_m/2$ is satisfied, while maintaining R within appropriate design limits. For R values in the range 0.18–0.21 mm, the corresponding simulated W_x values vary between 11.7 mm and 17 mm, which lie within the calculated interval of $[W_{x1}, W_{x2}]$=[11.5, 17.8] mm. The maximum lengths of the arrow-shaped slots, defined as $L_y + L_i$ for $i = 1, 2, 3, \ldots, 11$, were carefully selected to remain within the boundaries of the tapered slot region and were determined based on the upper limit of R. An additional constraint was imposed on the antenna's field characteristics, requiring the gain $G(\boldsymbol{x}, f)$ to remain at or above 9 dB for frequencies exceeding 17 GHz.

Accommodating the design goals mentioned requires an appropriate formulation of the merit function. Here, impedance matching is treated as a primary objective, whereas the gain constraint is handled using a penalty function approach (its explicit handling is inconvenient because it is an expensive constraint: its evaluation requires full-wave EM simulation of the antenna) [30]. The merit function $U(\boldsymbol{x})$ is defined as

$$U(\boldsymbol{x}) = \max_{f \in F} \{|S_{11}(\boldsymbol{x}, f)|\} + \beta \left[\frac{\max\{9 - G_{\min}(x), 0\}}{9} \right]^2 \tag{6}$$

where F is the frequency range of interest and

$$G_{\min}(x) = \min_{f \in F}\{|\ G(\boldsymbol{x}, f)\} \tag{7}$$

is the minimum in-band gain. The optimum solution $\boldsymbol{x}^*$ is identified by solving a nonlinear minimization task

$$\boldsymbol{x}^* = \arg\min_{x \in X} U(x) \tag{8}$$

Note that minimization of the function $U(\boldsymbol{x})$ improves the impedance matching, as well as enforces the condition imposed upon the antenna gain. The second term in (6) is proportional to the relative violation of the condition $G(\boldsymbol{x},f) \geq 9$ dB. The penalty coefficient is set to $\beta = 100$ [31], which ensures that gain violations exceeding a fraction of dB lead to a considerable contribution of the penalty term to U. Furthermore, the second power $[\ ]^2$ is used to facilitate exploration of the feasible region boundary (optimum designs are normally allocated at the boundary of that region).

The problem (8) is solved here using the trust-region (TR) gradient-based algorithm [32]. The sensitivities of the antenna response (specifically, its Jacobian matrix) are evaluated using finite differences [33]. The procedure yields approximations $\boldsymbol{x}^{(i)}$, i = 0,1, …, to $\boldsymbol{x}^*$ as

$$\boldsymbol{x}^{(i+1)} = \max_{\substack{x \in X \\ \|\boldsymbol{x}-\boldsymbol{x}^{(i)}\| \leq \boldsymbol{d}^{(i)}}} U_L^{(i)}(\boldsymbol{x}) \tag{9}$$

The objective function $U_L^{(i)}$ in (9) is analytically identical to (6); however, it is evaluated using a linear approximation model of antenna responses. For the reflection response, the model is defined as

$$L_{S_{11}}^{(i)}(\boldsymbol{x}) = S_{11}(\boldsymbol{x}, f) + \nabla S_{11}\left(\boldsymbol{x}^{(i)}, f\right).(\boldsymbol{x} - x^{(i)}) \tag{10}$$

For gain characteristic, we have

$$L_G^{(i)}(x) = G(\boldsymbol{x}, f) + \nabla G\left(\boldsymbol{x}^{(i)}, f\right).(\boldsymbol{x} - \boldsymbol{x}^{(i)}) \tag{11}$$

where $\nabla S_{11}(\boldsymbol{x}^{(i)},f)$ and $\nabla G(\boldsymbol{x}^{(i)},f)$ are the gradients of the reflection and gain responses at design $\boldsymbol{x}^{(i)}$ and frequency f. The size $d^{(i)}$ of the search region is adaptively adjusted at each algorithm iteration using the standard TR rules [32]. The termination condition is based on convergence in the argument ($||x^{(i+1)} - \boldsymbol{x}^{(i)}|| < \varepsilon$; here, $\varepsilon = 10^{-3}$) or shrinking the radius $d^{(i)}$ ($d^{(i)} < \varepsilon$).

The initial design $\boldsymbol{x}$ = [0.200 0.250 1.900 0.300 1.600 2.500 3.500 3.600 4.000 4.200 4.600 4.700 4.900 5.000 0.300 0.800]^T was determined through parametric studies. The optimized design obtained through optimization was $\boldsymbol{x}^*$ = [0.195 0.350 2.210 0.200 1.840 2.920 3.610 3.790 4.110 4.230 4.790 4.600 4.810 4.980 0.210 0.910]^T mm. Figure 2 compares the antenna's reflection coefficients prior to and following optimization, revealing a marked enhancement across the 8.4–42.8 GHz range. The gain after optimization is stable at approximately 10 dBi for frequencies above 17 GHz.

IV. AM-ENHANCED GAIN PERFORMANCE

Although the gain of the proposed Vivaldi antenna is satisfactory given its compact size, the considerable path loss at MMW frequencies necessitates additional gain enhancement to preserve signal integrity. To address this, the Modified Square Split-Ring Resonator (M-SSRR) AM array was integrated into the antenna substrate, positioned both between and in front of the flare openings along the upper edge in the xy-plane, as illustrated in Fig. 3. Specifically, six unit cells are placed between the flares, while a 6 × 6 array is embedded in the substrate above the antenna.

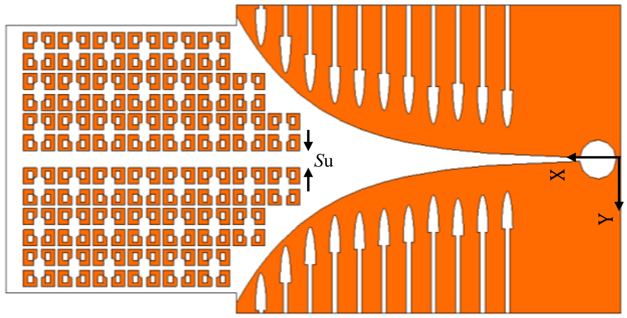

FIGURE 3. Configuration of the antenna integrated with AMs.

The number and placement of the M-SSRR unit cells were optimized through simulation to achieve an effective balance among gain enhancement, wide bandwidth, and compact antenna size. The unit cell separations along the x- and y-axes are set to 0.2 mm. In the central region, the spacing is increased to S_u = 0.45 mm to accommodate the slot that will host the second polarization antenna in the next stage of this work. The M-SSRR unit cell is developed through three sequential stages, as illustrated in Fig. 4(a)–(c). The initial configuration (Step 1) consists of a square resonator incorporating four identical gaps, g, symmetrically located at the midpoints of each side, thereby establishing the fundamental resonant response of the M-SSRR unit cell. In Step 2, vertical and horizontal metallic strips are introduced, extending inward from the edges of the peripheral gaps toward the center of the structure. These strips are deliberately terminated before reaching the center point to prevent physical contact or intersection. In the final stage (Step 3), a circular slot of radius, R_u, is etched in the central region of the unit cell. This modification is applied exclusively to the horizontal strips, introducing additional perturbation to the surface current distribution and enabling fine tuning of the resonant characteristics. The simulated S-parameters corresponding to the three design stages are presented in Fig. 4(d). Figure 4(c) illustrates the layout of the proposed M-SSRR structure, patterned on the front surface of the substrate, with specific dimensions provided in the figure caption. The primary purpose of this structure is to enhance the antenna's gain performance. Since the antenna radiates along the x-axis (end-fire direction), the ports were aligned accordingly. The boundaries were

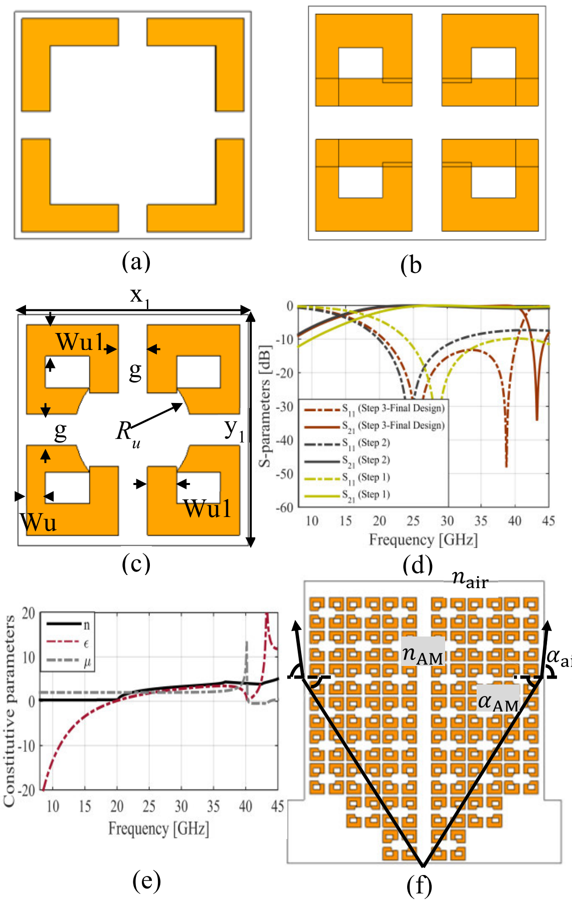

FIGURE 4. AM configuration and performance: (a) Initial design (Step 1); (b) intermediate design (Step 2); and (c) optimized final design with dimensions; x1 = 2.2 mm, y1 = 2 mm, Ru= 0.6 mm, Wu= 0.2 mm, Wu1= 0.3 mm, g=0.3 mm; (b) S-parameters; (c) Constitutive parameters; and (d) gain enhancement mechanism.

modeled as perfect electric (magnetic) conductors along the y(z) direction. The simulated S-parameters and the retrieved constitutive parameters of the proposed M-SSRR structure are presented in Figs. 4(d) and 4(e). The gain enhancement mechanism can be interpreted using Snell's law of refraction, expressed as $sin\alpha_{AM} \cdot n_{\mathrm{AM}} = sin\alpha_{\mathrm{air}} \cdot n_{\mathrm{air}}$ and $n_{\mathrm{AM}}(\alpha_{\mathrm{AM}})$ and $n_{\mathrm{air}}(\alpha_{\mathrm{air}})$ denote the refractive indices (angles) of the M-SSRR layer and air, respectively [18]. As illustrated in Fig. 4(f), when the incident angle α_{AM} is fixed, a higher refractive index n_{AM} produces a larger refractive angle α_{air}. Therefore, to achieve this property, the proposed M-SSRR structure must exhibit a refractive index greater than one ($n_{\mathrm{AM}} > 1$) at the desired frequency, cf. Fig. 4(e), enabling the transmitted energy to converge and focus on the radiation direction. Figure 5 presents the reflection coefficient and gain performance of the AM-based Vivaldi antenna. The incorporation of the AM array notably enhances the antenna gain above 20 GHz, achieving peak values of 13.3 dBi at 24 GHz and 38 GHz, compared to 10 dBi and 9.6 dBi, respectively, for the antenna without AMs, cf. Fig. 2. Additionally, the M-SSRR AM integration improves impedance matching, extending the operating bandwidth from 8.4–42.8 GHz (without AMs) to 8.3–45 GHz (with AMs). The bandwidth extension observed from 42.8 to 45 GHz is governed by the specific dispersive characteristics of the M-SSRR structure, as plotted in the constitutive parameters, cf. Fig. 4(e). Following the primary resonance at 40 GHz, the structure enters a Mu-Near-Zero (MNZ) state where permeability (μ) ≈0. This MNZ behavior effectively suppresses the reactive magnetic near-field energy, lowering the antenna's radiation Q-factor. Simultaneously, the effective refractive index, n, stabilizes in this upper-frequency window. This dispersionless behavior ensures a constant phase velocity, preventing extreme shifts in the effective electrical length and facilitating a continuous impedance match up to 45 GHz.

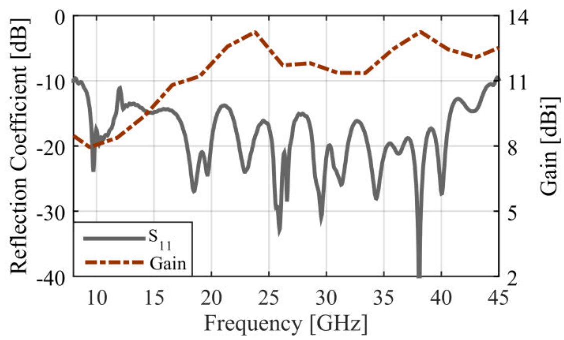

FIGURE 5. Reflection coefficient and gain of the antenna with AM array.

V. DUAL-POLARIZED SWB ANTENNA

The dual-polarized Vivaldi antenna configuration consists of two orthogonally oriented Vivaldi elements, as illustrated in Fig. 6. The second element is inserted through a precisely aligned slot located at the center of the first element's substrate, between its two flaring sections. This slot is formed exclusively in the dielectric substrate and does not intersect the copper radiating structure, which is offset by a distance of $s_d = 5.5$ mm from the minimum width (W_m) of the tapered slot. The resulting structure forms a compact dual-polarized radiator rather than a spatial array. By integrating two orthogonal radiators within a single aperture, the design enables polarization diversity through two co-located ports, providing dual-channel operation with reduced physical footprint and improved spectral utilization. This configuration is therefore well suited as a unit element for scalable integration into dual-polarized phased array systems. Moreover, the proposed architecture allows both elements to employ an identical feeding mechanism, significantly simplifying the overall design. By avoiding transmission-line crossover, the configuration eliminates the need for complex feed networks while preserving radiation performance and polarization purity. In addition, the interlocking arrangement facilitates straightforward fabrication, assembly, and practical implementation. The performance of the proposed antenna was evaluated using CST Microwave Studio. The simulated reflection coefficients, S_{11} and S_{22}, are presented

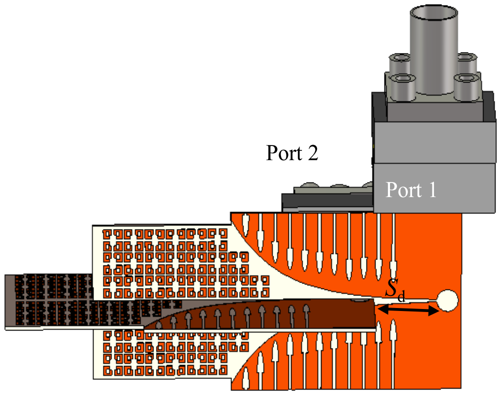

FIGURE 6. Configuration of the proposed dual-polarized Vivaldi antenna.

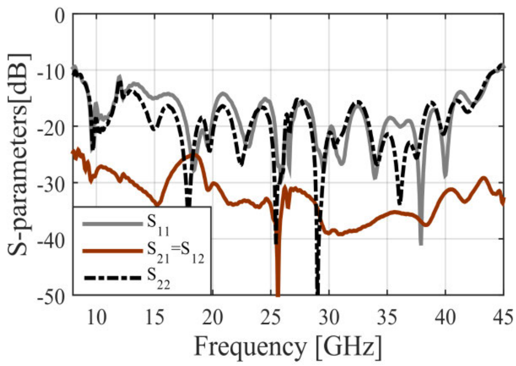

FIGURE 7. S-parameters of the dual-polarized Vivaldi antenna.

in Fig. 7. Both ports exhibit reflection values below −10 dB across the operating frequency band of 8.3–45 GHz, indicating performance comparable to that of a single AM-based Vivaldi antenna. This consistency is attributed to the almost symmetrical arrangement of the two antenna elements. A key advantage of this approach is the retention of the same feed structure and design parameters, unlike other designs that modify the feeding mechanism—often increasing complexity and leading to variations in S_{11} performance [25]. A slight discrepancy is observed, mainly due to the small height offset of the second element above the first, introduced to prevent feedline intersection and maintain proper isolation. The transmission coefficient is illustrated in Fig. 7, demonstrating high isolation exceeding 25 dB and exhibiting similar performance, with $S_{21} = S_{12}$ across both polarizations. Precise element placement and spatial offset effectively suppress mutual coupling. The proposed configuration demonstrates high gain with nearly identical performance for both polarizations, as shown in Fig. 8. This balanced gain response is particularly advantageous, as many existing designs exhibit noticeable gain discrepancies between polarizations due to asymmetrical arrangements, where one polarization often performs worse than the other—potentially limiting performance in polarization-sensitive applications. The simulated gain over the 17–45 GHz range varies between 10 dBi and 13.4 dBi, with peak values of 13.3 dBi and 13.4 dBi occurring at 24 GHz and 38 GHz, respectively.

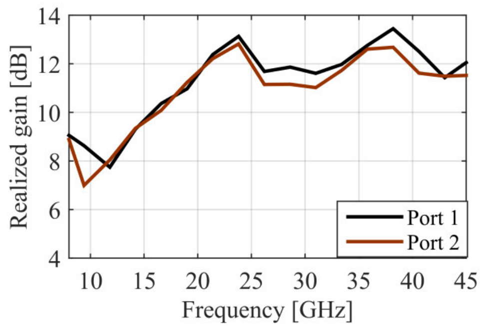

FIGURE 8. Gain performance of the antenna at both ports.

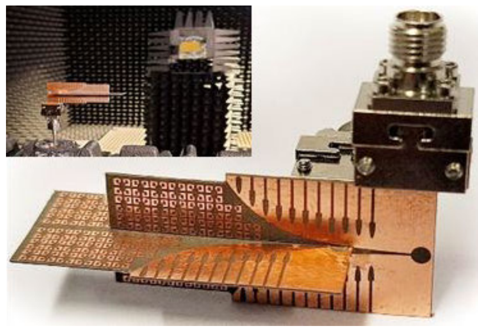

FIGURE 9. Fabricated prototype of the antenna, with an inset showing a close-up of the laboratory measurement setup.

VI. PERFORMANCE VALIDATION

A dual-polarized Vivaldi antenna incorporating M-SSRRs was fabricated based on the finalized optimized design and corresponding physical dimensions (cf. Fig. 9) to validate the simulated performance and demonstrate its suitability for remote sensing and 5G MMW systems. The operating frequency response was measured using an Anritsu MS4644B vector network analyzer, while the radiation characteristics were evaluated in an anechoic chamber, as shown in Fig. 9. The simulated and measured S-parameters are presented in Fig. 10, confirming the antenna's SWB performance and high isolation characteristics. The proposed design effectively spans a large portion of the microwave spectrum and extends into the MMW range (8.3–45 GHz), making it suitable for a wide range of applications. The reflection coefficients, S_{11} and S_{22}, shown in Figs. 10(a) and (b), demonstrate wide impedance bandwidth, while the measured transmission coefficient, S_{21}, shown in Fig. 10(c), confirms an isolation level exceeding 25 dB across the operational band. A good agreement is observed between the simulated and measured data for both the reflection and transmission coefficients, obtained using the MS4644B VNA, which supports measurements up to 40 GHz. Minor discrepancies are expected and can be attributed to fabrication tolerances, cable losses, and slight assembly inaccuracies. The realized gain performance of the system at both ports shows good agreement between simulated and measured results, as illustrated in Fig. 11. The simulated gain exhibits maxima of 13.3 dBi and 13.4 dBi occurring at 24 GHz and 38 GHz, respectively. The measured gain follows a similar trend and aligns closely with the simulation, with minor variations likely attributable to the same factors contributing to the discrepancies observed in the S-parameters. The simulated and measured efficiencies are presented in Fig. 12. The results indicate that the antenna maintains an efficiency exceeding 80% across the entire operating bandwidth, with values surpassing 90% in the 14–37 GHz range. The measured gain exhibits a similar trend and shows close agreement with the simulated results. Minor discrepancies, particularly around 40 GHz, can be attributed to fabrication tolerances, material uncertainties, and measurement setup limitations, consistent with the deviations observed in the S-parameter results.

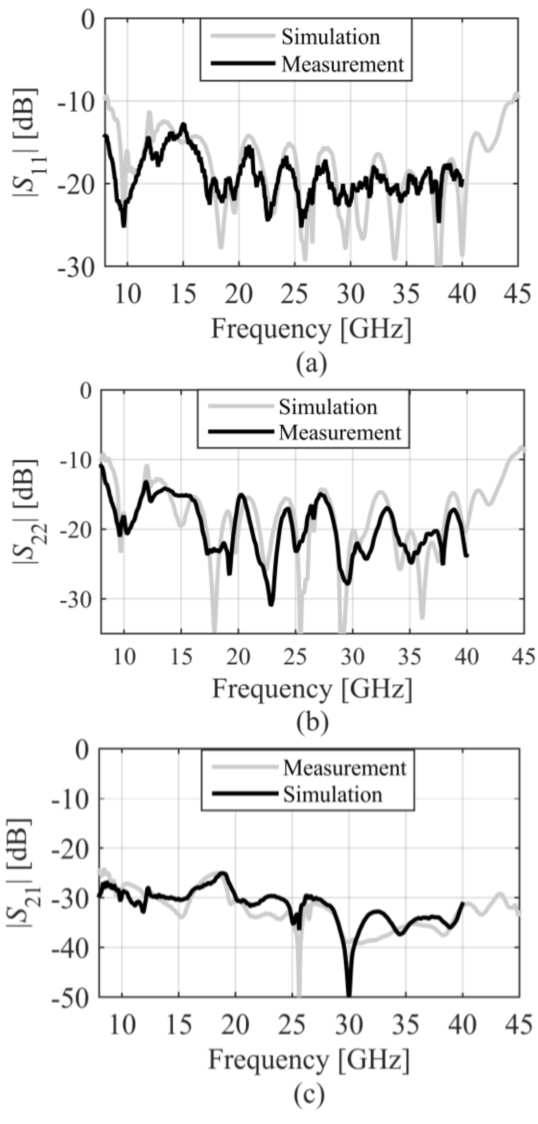

FIGURE 10. Simulated and measured S-parameters: (a)S_{11}, (b) S_{22}, and (c) S_{21}.

Figure 13 illustrates the radiation characteristics of the proposed dual-polarized antenna in the E- and H-planes

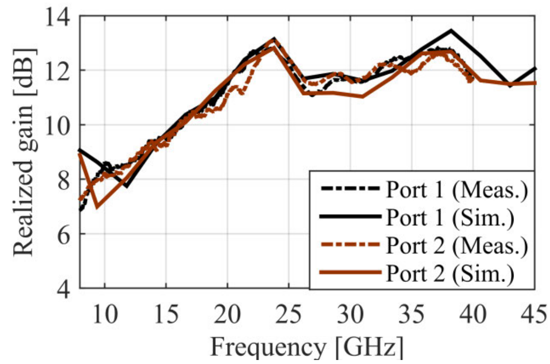

FIGURE 11. Simulated and measured gains.

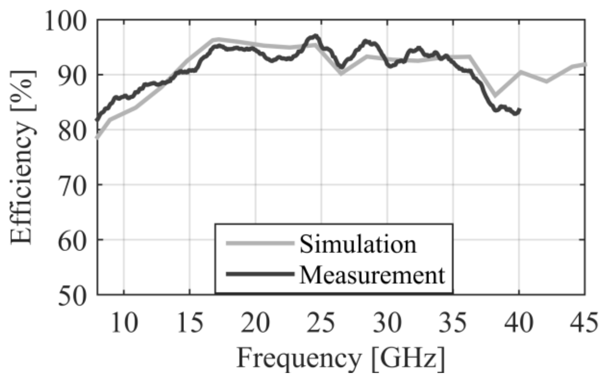

FIGURE 12. Simulated and measured efficiencies.

at 17.2 GHz, 24 GHz, and 38 GHz, with the radiation patterns for Port 1 and Port 2 shown individually. At all frequencies and for each port, the antenna exhibits directional radiation behavior, contributing to enhanced gain, reduced interference, and improved signal quality, the features essential for high-performance Ku-band remote sensing and MMW applications. The experimental results exhibit excellent agreement with the simulated data across both E- and H-planes at all frequencies. The cross-polarization levels remain below –20 dB, particularly at 17.2 GHz and 24 GHz. During the measurement process, the unused port was terminated with a 50-Ω matched load to ensure measurement accuracy.

VII. LINK BUDGET ANALYSIS

The performance of communication systems is largely determined by link budget analysis, which evaluates the range and reliability of the link. Communication quality is highly sensitive to degradation mechanisms such as reflection, path loss, polarization mismatches, and material absorption. To accurately evaluate the proposed system capabilities, it is essential to analyze the link between the antenna and the external receiving system across different distances. This assessment involves the application of well-established models to quantify antenna performance under realistic conditions. A critical outcome of this evaluation is the link margin (LM), a key performance metric that reflects the robustness of the

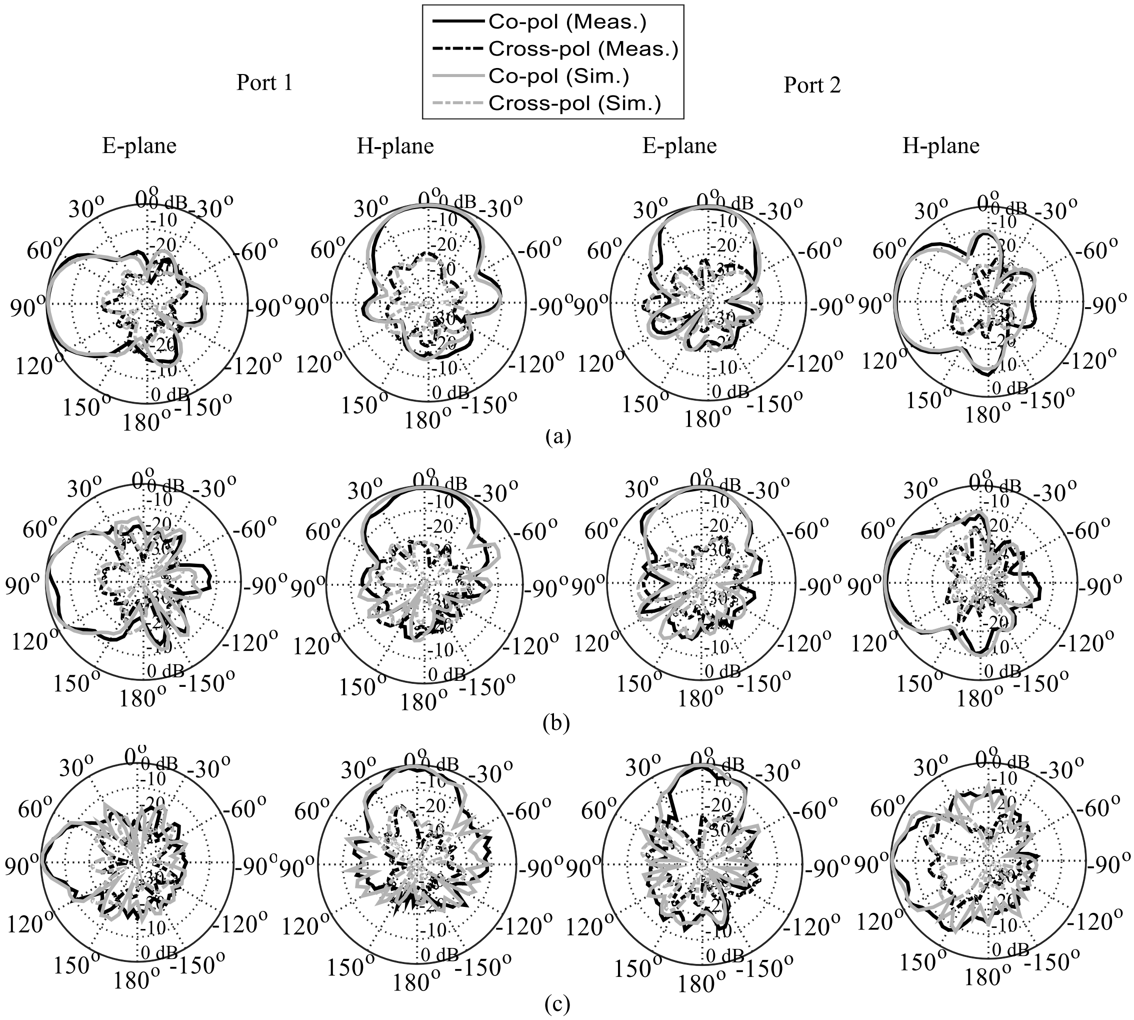

FIGURE 13. Co- and cross-polarization patterns in the E- and H-planes at (a) 17.2 GHz, (b) 24 GHz, and (c) 38 GHz.

communication link and determines whether the system can meet the required signal quality thresholds under varying propagation conditions. A positive LM indicates a reliable and stable wireless communication link [34]. The LM represents the difference between the actual received power and the minimum required power needed to maintain acceptable signal quality, and is expressed as:

$$LM = C_{\text{link}}/N_0 - C_{\text{req}}/N_0 \tag{12}$$

$$C_{\text{req}}/N_0 = E_b/N_0 + 10\log_{10}B_r - G_c + G_d \tag{13}$$

$$C_{\text{link}}/N_0 = P_t + G_t + G_r - L_{\text{FS}} - N_0 \tag{14}$$

where L_{FS} represents the free-space path loss, defined as

$$L_{\text{FS}} = 20\log_{10}(s) + 20\log_{10}(f) + 20\log_{10}(4\pi/c) \tag{15}$$

and N_0 is the noise power spectral density, expressed as

$$N_0 = 10\log_{10}(k) + 10\log_{10}(T) \tag{16}$$

$$T = T_0(NF - 1) \tag{17}$$

Here, s represents the distance between the transmitting and receiving antennas. In this study, Binary Phase Shift Keying (BPSK) modulation was employed, targeting a bit error rate (BER) of less than 1×10^{-5}, with data rates evaluated at 0.1 Gbps, 1 Gbps, and 3 Gbps. The LM was assessed at two carrier frequencies: 24 GHz and 38 GHz. The antenna gains for both the transmitter and receiver were assumed equal, with $G_t = G_r = 13.3$ dBi at 24 GHz and 38 GHz. The transmission distance s was considered up to 80 meters, and the reference temperature T_0 was set at 290 K. The energy-per-bit to noise power spectral density ratio (E_b/N_0) was set to be 9.6 dB, while the receiver noise figure was taken as 3.5 dB. The link budget performance was evaluated for data rates of 0.1 Gbps, 1 Gbps, and 3 Gbps, as illustrated in Fig. 14(a) and (b). These rates correspond to three standardized throughput tiers: 0.1 Gbps, representing a high-reliability baseline for remote sensing telemetry; 1 Gbps, corresponding to the standard IMT-2020 benchmark for 5G terrestrial services; and 3 Gbps, demonstrating the

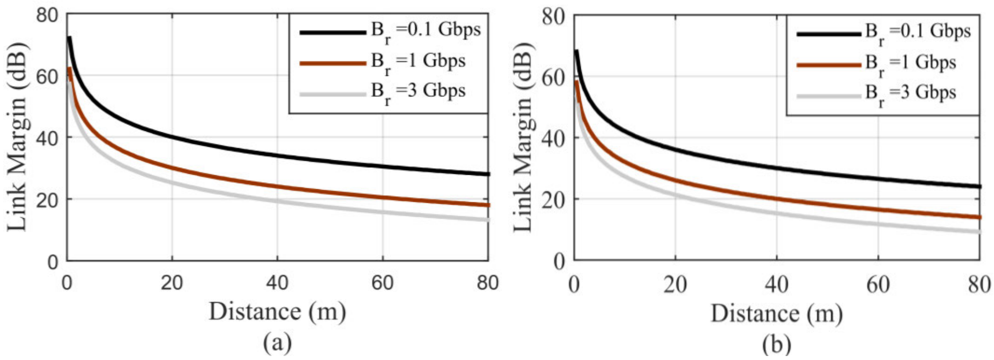

FIGURE 14. LM analysis at (a) 24 GHz and (b) 38 GHz.

TABLE 1. Performance comparison of the proposed dual-polarized antenna with recent literature.

Ref.	Antenna (Size (λ^3))	Frequency (GHz)	Max. Gain (dBi)	Isolation	Polarization	Gain enhancement Mechanism
[21]	1.12×1.12×0.07	1.4–2.1	10.5	–	single	MM array
[22]	2.6×1.3×0.02	13–20	12.4	–	single	MM array
[23]	1.48 × 0.96 × 0.02	3.7–25	11.8	–	single	MS array
[24]	0.9×0.41×0.02	22.5–45	8.5	> 20	dual	–
[25]	1.96×1.68×0.02	1.8–6	10	> 23	dual	–
[26]	0.54×0.54×0.12	23.5–30 36.7–47	13	> 14	dual	–
[2]	2.56×0.56×0.13	24–44	10	> 13	dual	–
[27]	1.28×1.28×0.95	5.08–6.4	8	> 17.5	dual	–
This work	0.94×0.49×0.01	8.3-45	13.3	> 25	dual	AMs array

system's capacity to support high-order modulation schemes required for transmitting uncompressed scientific data from high-resolution remote sensing payloads. The results reveal that the link margin decreases with increasing communication distance, and the lowest link margin occurs at the highest data rate, highlighting the trade-off between data speed and link reliability. As illustrated in Fig. 14(a), at 24 GHz, the proposed Vivaldi antenna maintains a 20 dB link margin across distances of 80 m, 60 m, and 40 m corresponding to data rates of 0.1, 1, and 3 Gbps, respectively. At 38 GHz (Fig. 14(b)), the antenna supports reliable communication links over distances of 80 m, 41 m, and 23 m for the same set of data rates.

Table 1 presents a comprehensive performance comparison between the proposed dual-polarized antenna and state-of-the-art designs reported in recent literature. In contrast to previous works, the proposed antenna achieves SWB operation with high gain and excellent polarization isolation, while maintaining a compact and low-profile configuration.

VIII. CONCLUSION

A compact, high-performance dual-polarized SWB antenna was presented in this work, developed using a staged design approach. Initially, a compact Vivaldi antenna was designed to achieve low-profile SWB operation. In the next stage, arrow-shaped slots were incorporated to enhance the bandwidth, followed by the integration of an M-SSRR array, which further improved both gain and bandwidth. Finally, a dual-polarization configuration was realized using two orthogonally oriented Vivaldi elements. The developed dual-polarized antenna operates over a wide frequency range of 8.3–45 GHz, achieving high polarization isolation exceeding 25 dB and high gain, with peak values of 13.3 dBi and 13.4 dBi at 24 GHz and 38 GHz, respectively. Covering the X-, Ku-, and K-bands, as well as key 5G NR MMW bands (n257–n261), the antenna is a promising candidate for 5G communications and satellite remote sensing applications. Compared with recent works, the design offers a simplified, low-profile solution that delivers SWB performance, high gain, and polarization diversity.

REFERENCES

[1] P. J. Gibson, "The Vivaldi aerial," in *Proc. 9th Eur. Microw. Conf.*, Mar. 1979, pp. 101–105.

[2] Q. Chen, J. Ala-Laurinaho, A. Khripkov, J. Ilvonen, R. M. Moreno, and V. Viikari, "A wideband dual-polarized endfire antenna array for 5G mm-Wave smartphones," *IEEE Trans. Antennas Propag.*, vol. 72, no. 2, pp. 1118–1127, Feb. 2024.

[3] B. A. F. Esmail, D. Isleifson, and L. Shafai, "A Ku-band compact offset cylindrical reflector antenna with high gain for low-Earth orbit sensing applications," *Sensors*, vol. 24, no. 23, p. 7535, Nov. 2024.
[4] J. Ran, Y. Wu, C. Jin, P. Zhang, and W. Wang, "Dual-band multipolarized aperture-shared antenna array for ku-/Ka-band satellite communication," *IEEE Trans. Antennas Propag.*, vol. 71, no. 5, pp. 3882–3893, May 2023.
[5] M. Nasir, A. Iftikhar, M. F. Shafique, B. Saka, S. Nikolaou, and D. E. Anagnostou, "Broadband dual-podal multilayer Vivaldi antenna array for remote sensing applications," *IET Microw., Antennas Propag.*, vol. 17, no. 7, pp. 505–517, Jun. 2023.
[6] H.-T. Chou and Y.-J. Lin, "An optimum design of paired balanced antipodal Vivaldi antennas with mirror-imaged symmetric architectures for ultra-broadband characteristics from microwave to millimeter-wave frequency ranges," *IEEE Access*, vol. 10, pp. 99516–99524, 2022.
[7] M. Vishwakarma, P. Nagaraja Rao, and S. Vuta, "A miniaturized double sided Vivaldi antenna with enhanced radiation traits for EW applications," *Prog. Electromagn. Res. C*, vol. 143, pp. 131–139, 2024.
[8] S.-W. Kim and D.-Y. Choi, "Implementation of rectangular slit-inserted ultra-wideband tapered slot antenna," *SpringerPlus*, vol. 5, no. 1, pp. 1–11, Dec. 2016.
[9] H. Zhang and F. Zhang, "A novel ultrawideband miniature Vivaldi antenna with sawtooth outer edges and inclined elliptical slots," *IEEE Antennas Wireless Propag. Lett.*, vol. 23, pp. 2708–2712, 2024.
[10] P. P. Kumar and P. Saxena, "High gain metamaterial loaded antipodal tapered slot antenna over 20–40 GHz for imaging applications," *AEU-nt. J. Electron. Commun.*, vol. 146, pp. 1–9, Jun. 2022.
[11] A. Muniyasamy and K. Rajakani, "UWB radar cross section reduction in a compact antipodal Vivaldi antenna," *AEU - Int. J. Electron. Commun.*, vol. 99, pp. 369–375, Feb. 2019.
[12] M. Bhagyalakshmi, L. S. L. Sowjanya, and N. N. Sastry, "Compact antipodal Vivaldi antenna with rectangular slots and shaping of flare to cover 6 to 18 GHz," *Electromagnetics*, vol. 38, no. 8, pp. 531–543, Nov. 2018.
[13] S. Pan, W. Shen, Y. Feng, Z. Liu, P. Xiao, and G. Li, "Miniaturization and performance enhancement of Vivaldi antenna based on ultra-wideband metasurface lens," *AEU - Int. J. Electron. Commun.*, vol. 134, May 2021, Art. no. 153703.
[14] J.-Y. Yang, X.-H. Ding, T.-Y. Yan, W.-W. Yang, Y. Li, and J.-X. Chen, "High-gain 60 GHz high-order-mode patch antenna array based on single-layer ridge gap waveguide," *IEEE Antennas Wireless Propag. Lett.*, vol. 24, pp. 878–882, 2025.
[15] D. Zarifi, A. S. Saber, and A. U. Zaman, "A high-gain gap waveguide-based 16×16 slot antenna array with low sidelobe level for mmWave applications," *Sci. Rep.*, vol. 14, no. 1, pp. 1–9, Dec. 2024.
[16] M. S. Shishkin, "Bandwidth enhancement methods analysis for high-gain stacked microstrip antenna," *Prog. Electromagn. Res. B*, vol. 107, pp. 19–31, 2024.
[17] H. Cho, J.-H. Lee, S. Kim, J.-W. Yu, and B. Ahn, "Series-fed integrated lens antenna for high gain in millimeter-wave band," *IEEE Antennas Wireless Propag. Lett.*, vol. 23, pp. 1578–1582, 2024.
[18] B. A. F. Esmail, S. Koziel, A. Pietrenko-Dabrowska, and D. Isleifson, "Wideband high-gain low-profile series-fed antenna integrated with optimized metamaterials for 5G millimeter wave applications," *Sci. Rep.*, vol. 14, no. 1, pp. 1–12, Jan. 2024.
[19] S. Zhu, H. Liu, P. Wen, L. Du, and J. Zhou, "A miniaturized and high gain double-slot Vivaldi antenna using wideband index-near-zero metasurface," *IEEE Access*, vol. 6, pp. 72015–72024, 2018.
[20] S. Kumar and A. S. Dixit, "Enhanced antipodal Vivaldi antenna with SSRR metamaterial for improved 5G performance in the 38 GHz band," *Results Eng.*, vol. 24, Dec. 2024, Art. no. 103133.
[21] H. Cheng, H. Yang, Y. Li, and Y. Chen, "A compact Vivaldi antenna with artificial material lens and sidelobe suppressor for GPR applications," *IEEE Access*, vol. 8, pp. 64056–64063, 2020.
[22] B. Liu, Y. Zhang, J. Lin, J. Zhuo, K. Lai, and L. Ye, "Endfire gain enhancement enabled by a modified antipodal Vivaldi antenna with metamaterials," *IEEE Photon. Technol. Lett.*, vol. 36, no. 23, pp. 1385–1388, Dec. 2024.
[23] M. F. Zambak, S. Johari, M. N. M. Yassin, A. M. Ismail, and A. Alghaihab, "Ultra-wide band antipodal Vivaldi antenna using metasurface lens for gain and front-to-back ratio (FBR) improvement," *Radio Sci.*, vol. 59, no. 10, pp. 1–15, Oct. 2024.
[24] A. Azari, A. Skrivervik, H. Aliakbarian, and R. A. Sadeghzadeh, "A super wideband dual-polarized Vivaldi antenna for 5G mmWave applications," *IEEE Access*, vol. 11, pp. 80761–80768, 2023.
[25] K. Zhang, R. Tan, Z. H. Jiang, Y. Huang, L. Tang, and W. Hong, "A compact, ultrawideband dual-polarized Vivaldi antenna with radar cross section reduction," *IEEE Antennas Wireless Propag. Lett.*, vol. 21, pp. 1323–1327, 2022.
[26] H. C. Ye, C. Mao, L. L. Dai, and X. Y. Zhang, "Dual-band dual-polarized antenna and array with enhanced bandwidth for 5G millimeter-wave applications," *IEEE Antennas Wireless Propag. Lett.*, vol. 24, pp. 1829–1833, 2025.
[27] A. R. Pitol, C. Müller, M. S. V. Arigony, C. M. Barth, and L. Gerhardt, "Compact dual-polarization quad-ridge horn," *IEEE Antennas Wireless Propag. Lett.*, vol. 22, pp. 3142–3146, 2023.
[28] S. Saleh, W. Ismail, I. S. Z. Abidin, M. H. Jamaluddin, M. H. Bataineh, and A. S. Alzoubi, "Compact UWB Vivaldi tapered slot antenna," *Alexandria Eng. J.*, vol. 61, no. 6, pp. 4977–4994, Jun. 2022.
[29] C. A. Balanis, *Antenna Theory: Analysis and Design*, 4th ed., Hoboken, NJ, USA: Wiley, 2016.
[30] S. Koziel, A. Pietrenko-Dabrowska, and M. Mahrokh, "On decision-making strategies for improved-reliability size reduction of microwave passives: Intermittent correction of equality constraints and adaptive handling of inequality constraints," *Knowl.-Based Syst.*, vol. 255, pp. 1–16, Nov. 2022.
[31] S. Koziel and A. Pietrenko-Dabrowska, "Reliable EM-driven size reduction of antenna structures by means of adaptive penalty factors," *IEEE Trans. Antennas Propag.*, vol. 70, no. 2, pp. 1389–1401, Feb. 2022.
[32] A. R. Conn, N. I. Gould, and P. L. Toint, *Trust Region Methods*. Philadelphia, PA, USA: SIAM, 2000.
[33] H. Levy and F. Lessman, *Finite Difference Equations*. New York, NY, USA: Dover, 1992.
[34] S. Khan, O. Khan, S. A. A. Shah, J. Nasir, B. T. Malik, S. Khan, and S. Koziel, "Highly compact wideband high-gain four-element MIMO antenna for 5G new radio IoT," *IEEE Internet Things J.*, vol. 12, no. 12, pp. 22350–22365, Jun. 2025.

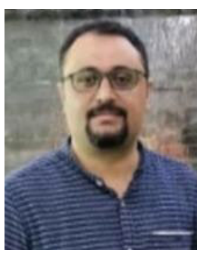

BASHAR A. F. ESMAIL (Member, IEEE) received the B.Eng. degree (Hons.) in electrical engineering (telecommunications) from Ibb University, Yemen, in 2008, and the M.Eng. and Ph.D. degrees in electrical engineering from Universiti Tun Hussein Onn Malaysia, Malaysia, in 2017 and 2021, respectively. In 2021, he joined the Engineering Optimization and Modeling Center (EOMC), Department of Electrical Engineering, Reykjavík University, Iceland, as a Postdoctoral Fellow. He is currently a Postdoctoral Researcher with the Department of Electrical and Computer Engineering, University of Manitoba, Canada. His research interests focus on the design and optimization of metamaterial structures, millimeter-wave antennas, MIMO systems, and reflector antennas for wireless and space applications.

DUSTIN ISLEIFSON (Senior Member, IEEE) received the Ph.D. degree in electrical and computer engineering from the University of Manitoba, Winnipeg, MB, Canada, in 2011. From 2013 to 2016, he was an Electrical Engineer with Magellan Aerospace, Winnipeg, where he worked on the Radarsat Constellation Mission (RCM). He has been with the Department of Electrical and Computer Engineering and the Centre for Earth Observation Science (CEOS), University of Manitoba, as an Assistant Professor, in 2016, and as an Associate Professor, in 2022. His research interests include remote sensing, Arctic science, antenna design, and satellite technologies. He is the Chapter Chair of the Winnipeg Section of the IEEE GRS/AES.

SLAWOMIR KOZIEL (Fellow, IEEE) received the M.Sc. and Ph.D. degrees in electronic engineering from Gdańsk University of Technology, Poland, in 1995 and 2000, respectively, the M.Sc. degree in theoretical physics and the M.Sc. degree in mathematics, in 2000 and 2002, respectively, and the Ph.D. degree in mathematics from the University of Gdańsk, Poland, in 2003. He is currently a Professor with the Department of Engineering, Reykjavík University, Iceland. His research interests include CAD and modeling of microwave and antenna structures, simulation-driven design, surrogate-based optimization, space mapping, circuit theory, analog signal processing, evolutionary computation, and numerical analysis.

ANNA PIETRENKO-DABROWSKA (Senior Member, IEEE) received the M.Sc. and Ph.D. degrees in electronic engineering from Gdańsk University of Technology, Poland, in 1998 and 2007, respectively. She is currently an Associate Professor with Gdańsk University of Technology. Her research interests include simulation-driven design, design optimization, control theory, modeling of microwave and antenna structures, and numerical analysis.